Rest-frame near-infrared radial light profiles up to z = 3 from JWST/NIRCam: Wavelength dependence of the Sérsic index

Martorano, M.; Wel, A. van der; Bell, E.F.; Franx, M.; Whitaker, K.E.; Nersesian, A.; ... ; Brammer, G.

The Astrophysical Journal, 957:46 (11pp), 2023 November 1 https://doi.org/10.3847/1538-4357/acf716

Rest-frame Near-infrared Radial Light Profiles up to $z = 3$ from JWST/NIRCam: Wavelength Dependence of the Sérsic Index

Marco Martorano[1], Arjen van der Wel[1], Eric F. Bell[2], Marijn Franx[3], Katherine E. Whitaker[4,5], Angelos Nersesian[1], Sedona H. Price[6], Maarten Baes[1], Katherine A. Suess[7,8], Erica J. Nelson[9], Tim B. Miller[10], Rachel Bezanson[6], and Gabriel Brammer[5]

[1] Sterrenkundig Observatorium, Universiteit Gent, Krijgslaan 281 S9, B-9000 Gent, Belgium; marco.martorano@ugent.be
[2] Department of Astronomy, University of Michigan, 1085 South University Avenue, Ann Arbor, MI 48109–1107, USA
[3] Leiden Observatory, Leiden University, P.O. Box 9513, 2300 RA, Leiden, The Netherlands
[4] Department of Astronomy, University of Massachusetts, Amherst, MA 01003, USA
[5] Cosmic Dawn Center (DAWN), Niels Bohr Institute, University of Copenhagen, Jagtvej 128, København N, DK-2200, Denmark
[6] Department of Physics and Astronomy and PITT PACC, University of Pittsburgh, Pittsburgh, PA 15260, USA
[7] Department of Astronomy and Astrophysics, University of California, Santa Cruz, 1156 High Street, Santa Cruz, CA 95064, USA
[8] Kavli Institute for Particle Astrophysics and Cosmology and Department of Physics, Stanford University, Stanford, CA 94305, USA
[9] Department for Astrophysical and Planetary Science, University of Colorado, Boulder, CO 80309, USA
[10] Department of Astronomy, Yale University, 52 Hillhouse Avenue, New Haven, CT 06511, USA
Received 2023 June 9; revised 2023 August 22; accepted 2023 September 4; published 2023 October 26

Abstract

We examine the wavelength dependence of radial light profiles based on Sérsic index n measurements of 1067 galaxies with $M_* \geqslant 10^{9.5}\,M_\odot$ and in the redshift range $0.5 < z < 3$. The sample and rest-frame optical light profiles are drawn from the Cosmic Assembly Near-infrared Deep Extragalactic Legacy Survey (CANDELS) and 3D Hubble Space Telescope (HST); rest-frame near-infrared light profiles are inferred from images collected for the Cosmic Evolution Early Release Science (CEERS) program with the Near Infrared Camera (NIRCam) on board of the James Webb Space Telescope (JWST). n shows only a weak dependence on the wavelength, regardless of the redshift, galaxy mass, and type. On average, star-forming galaxies have $n = 1$–1.5 and quiescent galaxies have $n = 3$–4 in the rest-frame optical and near-infrared. The strong correlation at all wavelengths between n and star formation activity implies a physical connection between the radial stellar mass profile and star formation activity. The main caveat is that the current sample is too small to discern trends for the most massive galaxies ($M_* > 10^{11}\,M_\odot$).

Unified Astronomy Thesaurus concepts: Galaxy structure (622); Galaxy evolution (594); Galaxy luminosities (603); Galaxy quenching (2040)

1. Introduction

James Webb Space Telescope (JWST) Near Infrared Camera (NIRCam) imaging is providing us for the first time with spatially resolved, rest-frame near-infrared (near-IR) structural information of galaxies at high redshift (up to $z \sim 3$) with an angular resolution unachievable from ground-based observatories. Previous extensive Hubble Space Telescope (HST) surveys have produced a detailed picture of the rest-frame UV and optical structural properties and their correlations with other galaxy properties such as the stellar mass and star formation rate (SFR; i.e., Lang et al. 2014; van der Wel et al. 2014a, 2014b; Shibuya et al. 2015; Nelson et al. 2016), but only at longer wavelengths is the stellar body revealed without being significantly hampered by the effects of stellar population and attenuation variations across galaxies.

The broad wavelength coverage together with the high angular resolution offered by the synergy between HST and JWST observations in the near-IR allows one to examine the wavelength dependence of the Sérsic index (n). For the first time we can determine for galaxies at large look-back time whether any trends in the rest-frame near-IR with stellar mass and star formation activity are substantially different from those seen in the rest-frame optical/UV.

Both nonparametric and parametric methods have been widely used to examine the galaxy structure; see Conselice (2014) for a comprehensive review on nonparametric methods and Whitney et al. (2021) for a recent application to high-redshift galaxies. Among parametric methods, Sérsic profile fits have become the standard as they are conveniently measured with codes such as GALFIT (Peng et al. 2002, 2010); this is the approach we use in this study.

As stellar populations and dust attenuation determine the light distribution, the measured structural properties are generally observed to depend on the wavelength (e.g., de Jong 1996a, 1996b; Kelvin et al. 2012; Häußler et al. 2013; Pastrav et al. 2013; Vika et al. 2013; Vulcani et al. 2014; Kennedy et al. 2015; Baes et al. 2020; Nersesian et al. 2023; Yao et al. 2023). Kelvin et al. (2012) used the low-redshift ($z < 0.3$) Galaxy And Mass Assembly (GAMA) survey (Driver et al. 2009) to examine the dependence of the Sérsic index on the wavelength, splitting the galaxy sample by visual morphology (disk galaxies and spheroidal galaxies). They find a mild dependence on the wavelength for spheroidal galaxies and a somewhat stronger correlation for disk galaxies. Kelvin et al. (2012) argue that the trend is to be expected, as spiral galaxies will have redder bulges, which tend to have $n > 1$. Despite this trend, the difference in the Sérsic indices between

disk and spheroidal galaxies persists even in the K_s band ($n \lesssim 2$ versus $n \approx 3.5$).

As the morphological class and structure/concentration (as parameterized by the Sérsic index) are intrinsically connected and, from an empirical perspective, derived from the same information, we will instead examine the wavelength dependence of the Sérsic index n separating galaxies by star formation activity, which is estimated independently from the Sérsic profile. Moreover, thanks to the revolutionary NIRCam imaging we can for the first time extend such an analysis to redshift $z = 2$ and beyond. The goal of this study is to measure the evolution of the Sérsic index with the redshift in the rest-frame near-IR and examine the wavelength dependence of the Sérsic index across the redshift range $0.5 < z < 3$. One question of specific interest is whether the difference between the Sérsic index for quiescent and star-forming galaxies, seen in the rest-frame optical (e.g., Blanton et al. 2003; Blanton & Moustakas 2009; Bell et al. 2012; Papovich et al. 2015), persists in the rest-frame near-IR. If not, then the star formation activity itself is the cause of the apparent difference in structure (while the underlying mass profile shows no such difference). Alternatively, if the difference persists, then there is a physical correlation between the shape of the radial stellar mass profile and star formation activity.

In this work we take advantage of the JWST/NIRCam (Rieke et al. 2005) imaging provided by the Cosmic Evolution Early Release Science (CEERS) program (Finkelstein et al. 2023) and model the light profiles of 1067 galaxies in the redshift range $z = 0.5$–3 with stellar masses $M_* \geqslant 10^{9.5} M_\odot$. We also compare our results with those of previous studies (Kelvin et al. 2012; van der Wel et al. 2012) to exploit the strengths and weaknesses of our study.

The paper is structured as follows. In Section 2 we describe the data sets used in this paper. Section 3 contains the results of this work divided into the different dependencies of Sérsic indices and a comparison with literature results. This is followed by a discussion in Section 4, and finally, in Section 5, we sum up the content of the paper and draw our conclusions.

We assume a flat ΛCDM cosmology with $H_0 = 70\,\mathrm{km\,s^{-1}\,Mpc^{-1}}$ and $\Omega_\mathrm{m} = 0.3$.

2. Data and Sample Selection

In this section we construct a redshift-selected and stellar-mass-selected sample from preexisting catalogs in the Extended Groth Strip (EGS; Davis et al. 2007) and derive Sérsic profile fits from the recently acquired JWST/NIRCam imaging from CEERS (Finkelstein et al. 2023).

2.1. Imaging and Photometry

Skelton et al. (2014) and Whitaker et al. (2014) presented HST, Spitzer, and ground-based imaging data to construct a widely used, homogeneous photometric catalog from the UV to 24 μm for the five extragalactic deep fields targeted by the Cosmic Assembly Near-infrared Deep Extragalactic Legacy Survey (CANDELS; Grogin et al. 2011; Koekemoer et al. 2011) and 3D-HST (Brammer et al. 2012), which Leja et al. (2020) used to estimate the redshift, stellar masses, SFRs, and dust attenuation parameters with the PROSPECTOR spectral energy distribution (SED) fitting code (Johnson & Leja 2017; Johnson et al. 2021). In this paper we use the Leja et al. (2020) catalog of redshifts, stellar masses, and SFRs for galaxies at redshift $0.5 < z < 3$.

We first crossmatch this catalog with van der Wel et al. (2012), which will be used as a reference for comparisons, and then with sources in the recent JWST/NIRCam data taken as part of the CEERS program (Finkelstein et al. 2017, 2023) in the EGS, one of the five CANDELS fields. We note (and correct for) a systematic shift in decl. of $+0\farcs19$ between the Skelton et al. (2014) coordinates and the coordinates in the CEERS mosaics, which we identified with the Python library for Source Extraction and Photometry SEP (Bertin & Arnouts 1996; Barbary 2016, 2018). We identify 2684 out of 63,413 galaxies in the Leja et al. (2020) catalog falling within the NIRCam footprint, of which 1216 are above our adopted stellar mass limit of $M_* = 10^{9.5} M_\odot$, which is the stellar mass completeness limit of the photometric catalog at $z \sim 3$ (Tal et al. 2014). 97% of these objects have signal-to-noise ratio (S/N) > 50 in all JWST/NIRCam filters, which is the requirement for unbiased Sérsic index measurements (van der Wel et al. 2012). This is not the case for the shallower HST Wide Field Camera 3 (WFC3) data, but those data do not play a major role in this work.

CEERS provides imaging in seven near-IR filters, specifically F115W, F150W, and F200W in the short-wavelength channel of NIRCam and F277W, F356W, F410M, and F444W through the long-wavelength channel. We use Stage 2b calibrated images already background subtracted available on the MAST archive additionally processed with the GRIZLI software (Brammer 2019) to obtain aligned imaging, weight, and segmentation mosaics out of the four pointings available when we started this work (also see Naidu et al. 2022).

For convenience, the available HST Advanced Camera for Surveys (ACS; F606W and F814W) and HST/WFC3 (F125W, F140W, and F160W) data are re-reduced with GRIZLI to produce mosaics that are aligned with the NIRCam mosaics from CEERS.

2.2. Sérsic Profile Fits

For each of the 1216 target galaxies with NIRCam imaging and for each of the seven JWST filters and five HST filters, we create square cutouts with size 10 times the effective radius in pixels measured from the F160W CANDELS imaging (van der Wel et al. 2012). We set a lower limit of 63 pixels ($\sim 2\farcs5$) and an upper limit of 200 pixels for sources with $m_\mathrm{F160W} > 22.5$. The upper limit is doubled for sources brighter than this threshold to ensure accurate background estimates. All objects in the cutout that are brighter than or less than 1 mag fainter than the target are assigned their own Sérsic profile and simultaneously fitted. All other sources in the van der Wel et al. (2012) catalog or in the CEERS segmentation map are masked.

We use GALFITM (Häußler et al. 2013; Vika et al. 2013) to perform the profile fits simultaneously for all JWST/NIRCam filters and simultaneously for all HST/ACS and HST/WFC3 filters. The model Sérsic profiles are convolved with the publicly available model Point-Spread Functions (PSFs)[11] drizzled with the same drizzle parameters as those used to create the mosaics. The square root of the inverse of the weight map is used as the noise map in GALFITM. The background, as well as the center of the galaxy, the total magnitude, Sérsic index, and effective radius are left as free parameters of the fit,

[11] https://github.com/gbrammer/grizli-psf-library/tree/main/ceers

allowing those to vary independently from filter to filter. The axis ratio and position angle are additional free parameters, but these are constrained to have the same value for all filters in the simultaneous fits.

We set the following constraints on the fit's parameters:

1. $0.2 \leqslant$ Sérsic index $\leqslant 12$
2. $0.01 \leqslant$ Re [pix] $\leqslant 150$
3. The x and y coordinates have to be within 5 pixels from the van der Wel et al. (2012) corrected position.

Following van der Wel et al. (2012), we assign a formal random uncertainty of 0.1 dex on the Sérsic index for objects with $S/N = 50$ and scale the (linear) uncertainty with $(S/N)^{-1/2}$. The S/N is calculated by summing the image and inverse weight maps across the object segment in the segmentation map.

In Figure 1 we show the data, model, and residual of four $10^{9.5}$–$10^{9.8}\,M_{\odot}$ galaxies at redshifts 0.74, 0.98, 2.49, and 2.98. Even these low-mass galaxies are detected with high significance and are well resolved by the JWST/NIRCam filters, even when HST does not.

In order to calculate the Sérsic index at specific rest-frame wavelength values we fit for each object a second-order Chebyshev polynomial to the independently measured Sérsic n values across all filters (but separately for JWST and HST to exploit differences between the instruments) with the uncertainties as weight factors. For each galaxy we fit the polynomial only to those filters where the galaxy was detected (i.e., does not fall in gaps of the NIRCam detectors) and with a converged value of n. We reject from our sample galaxies for which less than three filters are available to fit the polynomial. Among the JWST fits, just one galaxy does not satisfy this condition, while for the HST fits we reject 35 galaxies.

The adopted uncertainty for Sérsic indices at specific rest-frame wavelength recovered from the Chebyshev polynomial is that of the filter nearest in pivot wavelength. The differences between the directly measured Sérsic index values and the polynomial values are small, typically <5% and within the error bar.

We also remove from our sample those 113 objects for which the Sérsic index reached the $n = 0.2$ or $n = 12$ constraint for either of the JWST/NIRCam or HST/ACS filters. The WFC3 filters overlap in wavelength with the NIRCam/SW channel, so that such a rejection is not needed.

This leaves us with a final sample of 1067 galaxies in the redshift range $0.5 < z < 3$ and $M_* \geqslant 10^{9.5}\,M_{\odot}$. The rejected galaxies do not severely bias the sample as they do not occupy a particular region of the parameter space in terms of redshift or stellar mass (in the Appendix we show the stellar mass and specific SFR (sSFR) distribution of the selected sample and of the rejected galaxies as a function of the redshift).

To check whether the size adopted for cutouts is large enough to properly retrieve Sérsic profiles, we compare our size measurements with those presented in van der Wel et al. (2012) finding no systematic differences.

To ensure that the background estimate converges for the sizes of the cutouts, we compare the magnitudes with those obtained from cutouts half the size and, for a subset of the 50 most massive galaxies, the magnitudes obtained with cutouts double the size. From this exercise we conclude that the magnitudes are accurate to within 0.05 mag (and Sérsic indices to within 0.03 dex), indicating the systematic uncertainties in the background estimates do not play a significant role. To check for spatial variations of the background within cutouts we compared the standard deviation of pixels in the residuals with the median value in the noise maps, finding a good agreement between the two. This confirms that background spatial variations due to close bright sources or diffuse halos do not contribute significantly to the uncertainties.

Likewise we test whether constraining the position angle and axis ratio to the same value for all filters leads to systematic errors. With those parameters free to vary from filter to filter we find only small scatter in the Sérsic index n.

To test the reliability of our new HST-based Sérsic profile fits we compare in the upper panel of Figure 2 our measurements of Sérsic index in the HST/WFC3 filter F160W with the previously published values from van der Wel et al. (2012) inferred from the same data. Due to slight differences in the segmentation of objects and in methodology, there is scatter and a fair number of outliers appear (≈30% of the sample have $\Delta\log(n) > 0.08$ dex with no preferred properties, where $\Delta\log(n)$ is defined as $|\log_{10}(n_{\mathrm{F160W(vdw2012)}}) - \log_{10}(n_{\mathrm{F160W}})|$), but the systematic offset is negligible and the 1σ scatter is small (∼16%). Galaxies with $\Delta\log(n) > 0.08$ dex are characterized by a median S/N_{F160W} that is half of that of galaxies with smaller $\Delta\log(n)$, suggesting that low S/N might be an important source of scatter in this plot.

In the bottom panel of Figure 2 we show a comparison of NIRCam/F150W and HST/F160W Sérsic indices retrieved in this work. From this figure, we can infer that despite being shallower than JWST/F150W, HST/F160W was already deep enough to properly recover Sérsic indices for the whole population (van der Wel et al. 2012; Nedkova et al. 2021). Indeed, quantitatively, n_{F150W} is just ∼7% systematically larger than n_{F160W}. However, the large scatter observed reflects how the improved depth of F150W highlights new features that can change the Sérsic index of some galaxies. An example of such differences can be observed in the last two panels of Figure 1.

The scatter is larger by about a factor 2 compared to what one expects based on the formally adopted measurement uncertainties: the total uncertainty (on the ratio of the two independently measured Sérsic indices shown in the figure) is as much as 50%. That said, the random uncertainties on the CEERS-based measurements are typically a factor 3–4 smaller than those from CANDELS due to the increased S/N, leading us to conclude that the CEERS-based measurements have a variance that is one-quarter of the total variance seen in Figure 2. The error budget is an important issue that needs to be examined in detail, but it is also beyond the scope of this paper. Future improvements in the PSF model and background subtraction techniques are certain to improve the data analysis.

To test whether the choice of the PSF used to fit the NIRCam mosaics affects our results, we repeat the profile fits with an empirical PSF: a star visually identified in the NIRCam mosaics. The star is chosen to be faint (and therefore noisy) in order to avoid the well-known saturation issues in the NIRCam imaging (for an in-depth analysis of the JWST/NIRCam PSF, see, e.g., Nardiello et al. 2022; Weaver et al. 2023; Zhuang & Shen 2023). The difference between the model and the empirical PSFs is most pronounced in the short-wavelength channel, where we see a decrease of ∼25% in n for objects with $n > 3$. Low-n and long-wavelength-channel estimates are not systematically affected. This bias does not introduce large

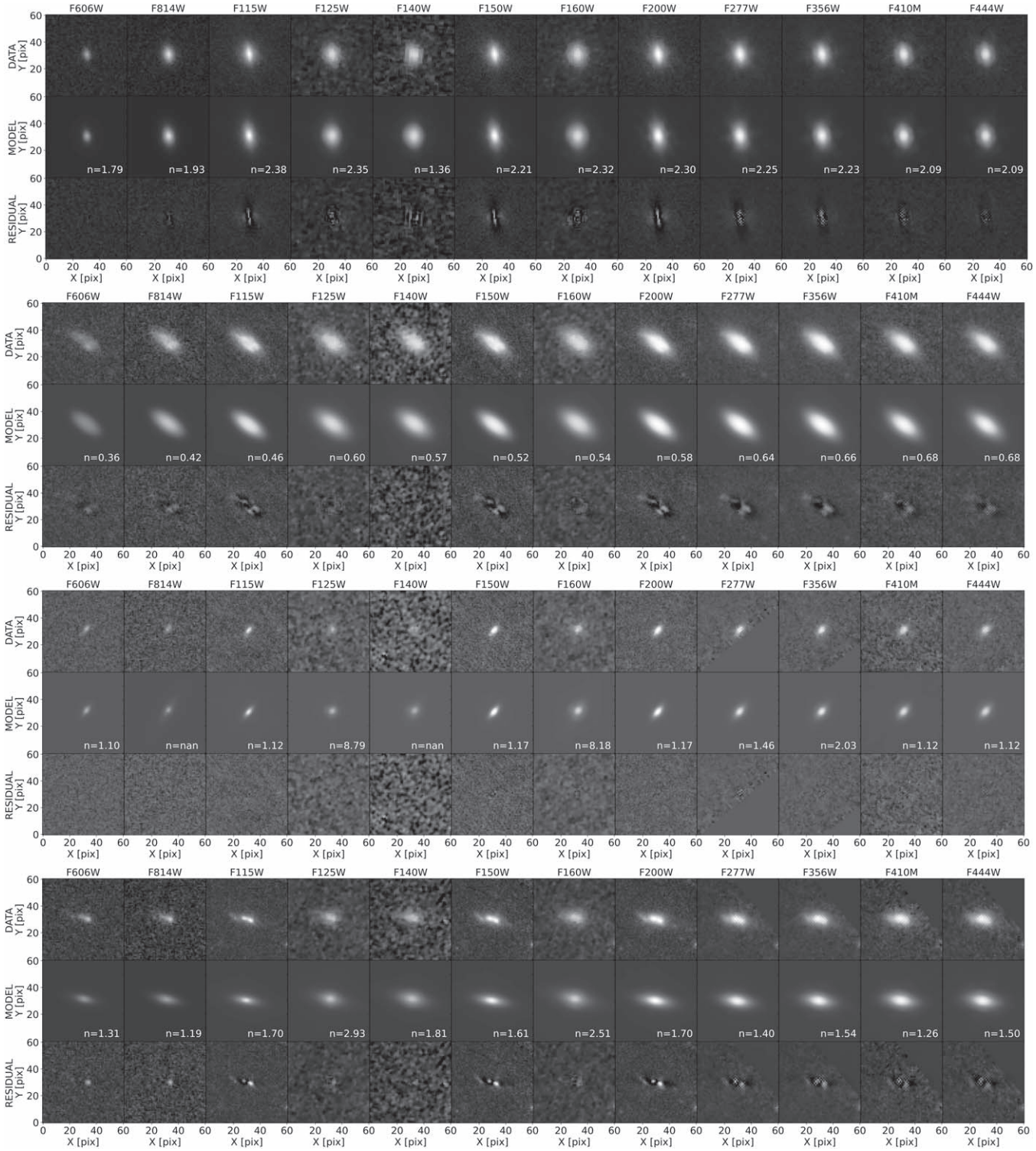

Figure 1. First panel: Galaxy 5751 in the Leja et al. (2020) catalog with $M = 10^{9.84}\,M_{\odot}$ and redshift $z = 0.74$; second panel: Galaxy 11438 with $M = 10^{9.60}\,M_{\odot}$ and redshift $z = 0.98$; third panel: Galaxy 10662 with $M = 10^{9.53}\,M_{\odot}$ and redshift $z = 2.49$; fourth panel: Galaxy 14128 with $M = 10^{9.60}\,M_{\odot}$ and redshift $z = 2.98$. For each of the four sets, the first row shows the original image, the second row the model used, and the third row the residuals. Per each galaxy the color of the panels spans the same scale in all the filters. Cutouts have been cropped with respect to those adopted for the fit to enhance galaxy visibility. Together with the model, in the bottom right corner, is shown the measured Sérsic index in each filter. In case that the fit of a filter failed, the value of Sérsic index reported is *nan*.

significant uncertainties in the following analysis and our conclusions do not depend on the choice of PSF. Solid dark (light)-gray lines show linear regression fits to the n values inferred with the model (empirical) PSF, using 3σ clipping. The empirical PSF results show systematic offsets at low and high n, whereas the model PSF results do not, implying that they suffer less from systematic uncertainties. The results based on the model PSF are used in the remainder of this paper.

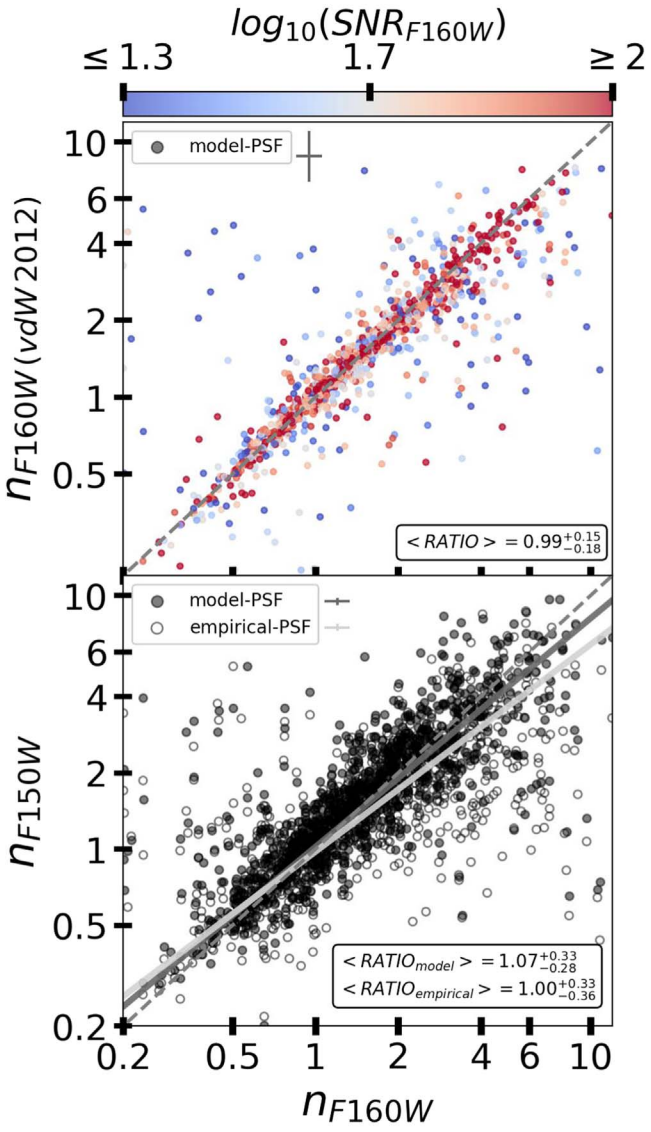

Figure 2. Upper panel: comparison between the HST/F160W Sérsic indices from van der Wel et al. (2012; *y*-axis) and the HST/F160W Sérsic indices derived in this paper (*x*-axis) color coded by the $\log_{10}$(S/N). Lower panel: comparison of the Sérsic indices from the JWST/NIRCam filter F150W and HST/WFC3 filter F160W (this paper). Filled circles represent F150W estimates with the WebbPSF-based model PSF while open circles show F150W estimates with the empirical PSF. Dark-gray and light-gray solid lines show linear fits, respectively, of the model PSF and empirical PSF data sets after 3σ clipping. In the lower right corner of each panel are reported the median ratios and the 16–84th percentile intervals. Next to the legends we show the median uncertainties. The first panel shows that the agreement with literature results is remarkable, while the second highlights how differences between the empirical and model PSFs arise mostly for high values of *n*.

2.3. Local Comparison Sample from GAMA

A $z \leqslant 0.3$ comparison sample is drawn from GAMA. For the GAMA I data set we use the GALFITM profile fits obtained from the SDSS *ugriz* imaging and UKIDSS-LAS YJHK imaging (Lawrence et al. 2007, 2012).[12]

MAGPHYS (da Cunha et al. 2008) stellar mass and SFR estimates from GAMA II[13] are used to construct the comparison sample of ~23,600 galaxies with $M_* \geqslant 10^{9.5}\,M_\odot$ and redshift $z \leqslant 0.3$. There may be systematic differences between MAGPHYS and PROSPECTOR-based parameter estimates, for the purpose of this study these are not significant. We study trends with mass and bulk redshift evolution so that 0.1–0.2 dex differences in M_* and the SFR do not matter.

3. Results

In this section we investigate the wavelength and mass dependence and redshift evolution of the Sérsic index, based on the 1067 galaxies in the redshift range $0.5 < z < 3.0$ and with stellar masses $M_* \geqslant 10^{9.5}\,M_\odot$, and the low-*z* comparison from GAMA. We often use the rest-frame 0.5 μm and 1.1 μm Sérsic index, $n_{0.5\mu m}$ and $n_{1.1\mu m}$, to examine the differences between rest-frame optical and rest-frame near-IR trends, choosing 0.5 μm to avoid the larger scatter at shorter wavelength, and choosing 1.1 μm to have common wavelength coverage across the entire redshift range.

3.1. Wavelength Dependence of the Sérsic Index n

We divide the sample into quiescent and star-forming galaxies defining the former as those galaxies that are located 0.8 dex below the SFR–M_* ridge defined by Leja et al. (2022; see also the Appendix). The ridge definition presented in Leja et al. (2022) applies to $0.2 < z < 3$ galaxies. The SFRs of GAMA galaxies at $z < 0.2$ are compared with the cutoff value for $z = 0.2$ to avoid extrapolation.

Figure 3 shows the median Sérsic index *n* as a function of the rest-frame wavelength. The medians (and percentile ranges) are constructed as follows. At a specific rest-frame wavelength all galaxies (minimum 10) with coverage from either HST or JWST are included using the Chebyshev polynomial value (see Section 2.3). If both HST and JWST cover that wavelength, JWST is preferred on account of its higher S/N. Lines are drawn using the COBS (Ng & Maechler 2007, 2022) library, which allows for a combination of a spline regression and quantile regression (the smoothing factor is chosen using the Schwarz-type information criterion automatically computed by the code).

We recover a clear, overall difference in the median Sérsic index of star-forming and quiescent galaxies: 1.36 ± 0.01 versus 3.28 ± 0.03, respectively (as indicated by the gray dashed lines in Figure 3). Uncertainties are computed as the standard deviation of 1000 replica of the medians computed at different wavelength and Gaussian distributed according to their own statistical uncertainty (represented by the error bars in Figure 3). Neither the quiescent nor the star-forming population shows a strong wavelength dependence across 0.3–2 μm. The scatter in *n* among all the galaxies, shown in the figure by means of the shaded areas that extend from the 16th to the 84th percentiles, is constant with wavelength for quiescent galaxies, but for star-forming galaxies the scatter decreases with the wavelength, likely due to a reduced variation in the radial profiles due to stochasticity in the distribution of young stars and dust. This reduced scatter at long wavelengths implies that the contrast between quiescent and star-forming galaxies is, statistically speaking, more significant in the near-IR than in the UV/optical.

The fact that the wavelength dependence is weak for the ensemble of galaxies does not necessarily imply that individual galaxies have similar Sérsic indices at all wavelengths. In

[12] http://www.gama-survey.org/dr4/schema/table.php?id=578
[13] http://www.gama-survey.org/dr4/schema/table.php?id=545

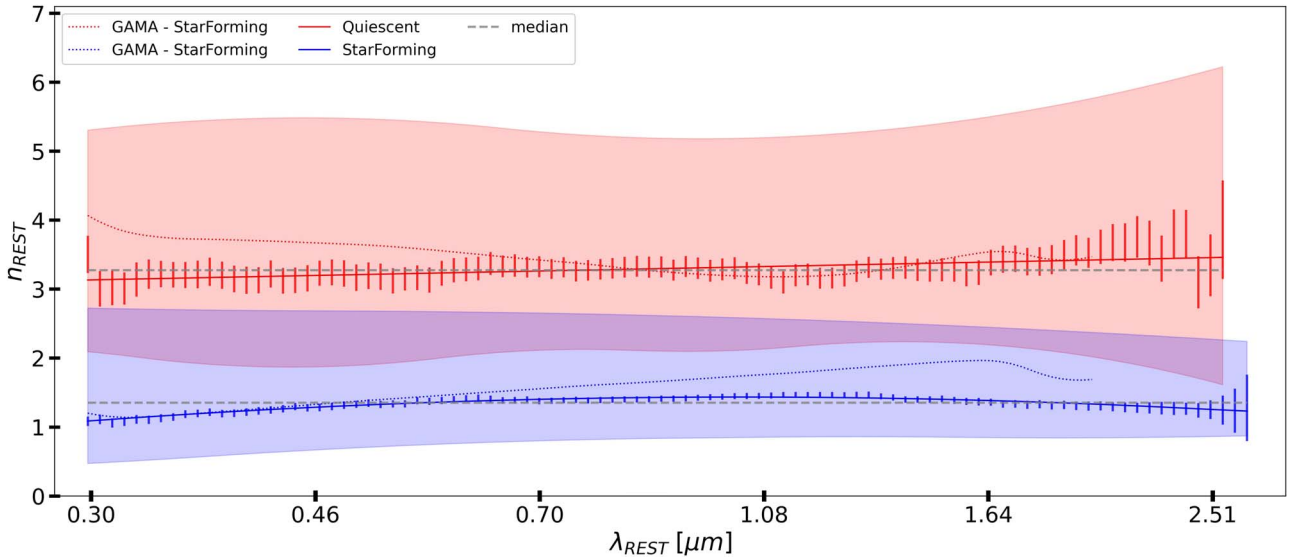

Figure 3. Median Sérsic index (and 16–84th percentile ranges as shaded areas) of the quiescent and star-forming population as a function of the rest-frame wavelength. Error bars indicate the statistical uncertainty in the median ($\sigma_n/\sqrt{N}$) at log-spaced wavelengths. Solid lines show a spline regression to the medians as outlined in the text. Dashed gray horizontal lines represent the overall median, integrated over the wavelength. The dotted lines show the low-z GAMA comparison sample. For both star-forming and quiescent galaxies we see no strong change in n with $\lambda_{\rm REST}$ from the near-UV to the near-IR.

Figure 4 we investigate the direct comparison between $n_{1.1\mu m}$ and $n_{0.5\mu m}$. The comparison shows only 0.1 dex (26%) scatter, which is a combination of observational uncertainties and physical variations. 19% of galaxies change their Sérsic index by more than a factor 1.5 (up or down) from 0.5 to 1.1 μm. The vast majority of galaxies have similar radial light profiles at different wavelengths. The fractions of galaxies with $n_{1.1\mu m}/n_{0.5\mu m} > 1.5$ and $n_{0.5\mu m}/n_{1.1\mu m} > 1.5$ are similar: 8% and 11%, respectively. At low n there is a small but significant deviation in the sense that $n_{0.5\mu m}$ is smaller than $n_{1.1\mu m}$, driven by galaxies with large A_V. We performed a Cramér test (Baringhaus & Franz 2004) to asses whether $n_{0.5\mu m}$ and $n_{1.1\mu m}$ share the same distribution. For quiescent galaxies the test result is 0.34 with an estimated p-value of 0.89 (with a 1σ confidence interval), confirming the absence of wavelength dependence on the Sérsic index for quiescent galaxies. On the contrary, for star-forming galaxies, we find an observed statistic of 3.75 with a p-value of 10^{-3}, suggesting that the Sérsic index indeed shows a mild dependence on the wavelength. However, as shown in the bottom panel of Figure 4, $n_{0.5\mu m}/n_{1.1\mu m}$ becomes systematically smaller than unity for increasing A_V. To statistically confirm this observation we performed a Cramér test on those star-forming galaxies with $A_V < 0.3$ finding that $n_{0.5\mu m}$ and $n_{1.1\mu m}$ for these galaxies are distributed the same (test result 0.64, p-value 0.36). This is consistent with the recent results from Gillman et al. (2023) who find that submillimeter-selected galaxies (expected to be dusty) have more concentrated profiles in the rest-frame near-IR than in the rest-frame optical/UV.

Figure 3 shows also the wavelength dependence of the Sérsic index for the $z \leqslant 0.3$ comparison sample drawn from GAMA (Section 2.3). Although the star-forming galaxies show an increase with the wavelength from $n = 1$ to almost $n = 2$ in the rest-frame H band, or ≈45% higher than seen in the high-z sample, the quiescent population shows a milder evolution with its peak in the near-UV. The trend shown by the star-forming galaxies echoes the findings by Kelvin et al. (2012) for GAMA, but they divided the sample into disk and spheroidal classes, presenting a different look compared to our separation by star formation activity. It is worth pointing out that the definition of quiescence can be important: different definitions can affect the strength of the increase(decrease) in the near-IR(near-UV) shown by star-forming(quiescent) galaxies. Definitions like that presented in Tacchella et al. (2022; where a galaxy starts its quiescent phase when sSFR $< 1/(3t_H(z))$, with $t_H(z)$ being the age of the universe at the galaxy's redshift) lead to much shallower slopes for both the GAMA quiescent and star-forming population leaving almost unaffected our high-redshift sample.

Nonetheless, the good agreement between the two data sets suggests a lack of dependence on redshift for the quiescent population and a mild evolution in the median n for the star-forming population.

The trends shown in Figure 3 are for the full galaxy sample, with a wide range in redshift and stellar mass. Correlations with the star formation activity, stellar mass, and redshift will be examined in further detail in Sections 3.2 and 3.3.

3.2. Correlations with the Star Formation Activity

Figure 3 suggests that the star formation activity shows a strong correlation with the Sérsic index, regardless of the wavelength. In Figure 5 we show $n_{1.1\mu m}$, the Sérsic index at rest-frame 1.1 μm, as a function of the sSFR. Lines are drawn with the technique presented in Section 3.1. The smoothing factor is chosen using the Schwarz-type information criterion. Galaxies with low sSFR have systematically larger $n_{1.1\mu m}$ than galaxies with high sSFR. For both $n_{1.1\mu m}$ and $n_{0.5\mu m}$ the Cramér test excludes, with very high confidence of $<5\sigma$, the possibility that star-forming and quiescent galaxies are drawn from the same n distribution. However, star-forming galaxies show a tail of high-n galaxies. This echoes earlier results obtained in the rest-frame optical by Bell et al. (2012) and Whitaker et al. (2017), who argued that having a high Sérsic index is a necessary, but not sufficient, condition for a galaxy to be quiescent.

Interestingly, the Sérsic index does evolve with the redshift at fixed sSFR; galaxies with $\log(\mathrm{sSFR}) \sim -10$ have $n_{1.1\mu m} \lesssim 2$ at $z \sim 1$ and $n_{1.1\mu m} \sim 3$ at $z \sim 2$. Rather than indicating a physical decrease in $n_{1.1\mu m}$ with cosmic time, this should be interpreted in the context of a decline in the SFR with cosmic

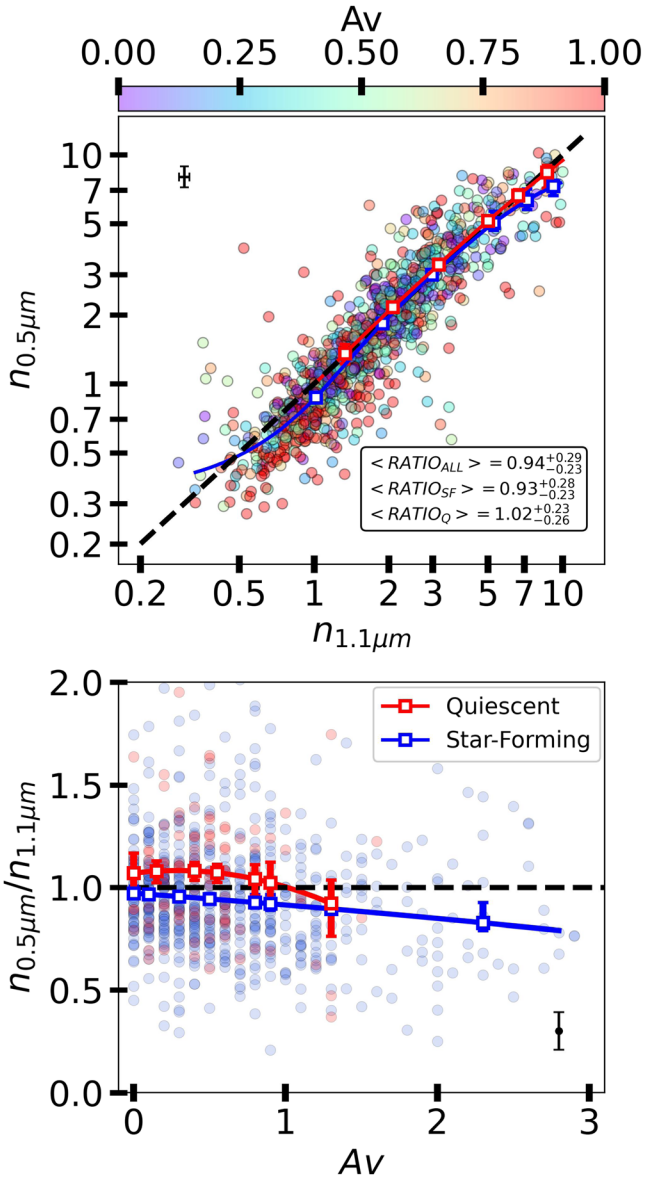

Figure 4. Upper panel: Sérsic index at 0.5 μm against Sérsic index at 1.1 μm color coded with A_V (from the PROSPECTOR SED fits). Blue and red solid lines show the median for star-forming and quiescent galaxies, respectively, computed as explained in the text. Error bars show the statistical uncertainty (84–16th percentiles $/\sqrt{N}$). In the lower right corner is shown the median (and 16–84th percentiles) ratio $n_{0.5\mu m}/n_{1.1\mu m}$ for the whole sample, the star-forming population and the quiescent population. In the upper left corner in black are shown the median uncertainties. Lower panel: ratio between Sérsic index at 0.5 and 1.1 μm against A_V. Only galaxies with S/N > 100 are included in this figure to highlight the trend with A_V. In the lower right corner in black is shown the median uncertainty propagated to the ratio of Sérsic indices.

time, which is of course well documented (Leja et al. 2022, and references therein).

We also see that galaxies with low sSFRs do not show a difference between $n_{1.1\mu m}$ and $n_{0.5\mu m}$. On the contrary, at $z < 1.5$ (left panel of Figure 5) high-sSFR galaxies show positive values of $n_{1.1\mu m}/n_{0.5\mu m}$. At $z > 1.5$ there is no such trend, but there is a significant scatter in $n_{1.1\mu m}/n_{0.5\mu m}$, which is mostly due to variations in $n_{0.5\mu m}$ (rather than $n_{1.1\mu m}$); otherwise this would result in a vertical gradient in the color coding. This scatter does not reflect difficulties in estimating the Sérsic profiles at 0.5 μm at high redshift as these come from high-S/N JWST/NIRCam imaging, but rather a wider variety of $n_{0.5\mu m}$ values at high redshift, likely due to variance induced by bright star-forming regions and/or dust-obscured areas.

3.3. Correlations with the Stellar Mass

The wavelength and sSFR dependence of the Sérsic index shown above does not consider any correlation with the stellar mass. Figure 6 shows $n_{1.1\mu m}$, $n_{0.5\mu m}$ and their ratio as a function of the stellar mass. Regardless of the wavelength, the Sérsic index increase with the stellar mass is in part due to the underlying correlations between, on the one hand, the stellar mass and sSFR, and on the other hand the sSFR and Sérsic index. Additionally, among quiescent galaxies, the Sérsic index increases with the stellar mass, while for star-forming galaxies such an increase is less evident. Here we should keep in mind that the current sample has only a few massive star-forming galaxies with significant bulge components.

Regardless of the detailed mass dependencies that may exist, the main point is that the Sérsic index—stellar mass distribution looks very similar in the rest-frame optical and rest-frame near-IR, and that these patterns exist across the entire redshift range $0.5 < z < 3$. This is further elucidated by the bottom panels that show $n_{1.1\mu m}/n_{0.5\mu m}$, which does not deviate much from unity across the sampled stellar mass range. The only significant departure is seen, somewhat surprisingly, for lower-M_* star-forming galaxies at $z < 1.5$, which have slightly higher $n_{1.1\mu m}$ than $n_{0.5\mu m}$. These galaxies often have $n_{0.5\mu m} < 1$ whereas $n_{1.1\mu m} \approx 1$, which may suggest that these galaxies have diffusely distributed young populations and/or somewhat attenuated centers, while the underlying populations have approximately exponential profiles.

In the highest redshift bin we observe that the median $n_{1.1\mu m}/n_{0.5\mu m}$ is compatible with unity for star-forming galaxies with $M_* < 10^{10.3}\,M_\odot$ followed by an increase that peaks at $M_* \sim 10^{10.7}\,M_\odot$ and a sharp decline for higher masses. The quiescent population shows no significant trend. However, the sample is too small at these high masses to claim a physical difference in $n_{1.1\mu m}/n_{0.5\mu m}$.

4. Discussion

While light profiles in the optical/UV can be strongly affected by young stars and dust absorption, the near-IR is more representative of the stellar mass distribution. However, the striking absence of a strong wavelength dependence of the Sérsic index n for both quiescent and star-forming galaxies over the redshift range $0 < z < 3$ suggests that the curvature of the radial light profile in the optical does not deviate much from that of the underlying stellar mass distribution across most of cosmic time. An exponential profile at short wavelengths predicts an exponential profile at long wavelengths, and a De Vaucouleurs-like profile generally also persists across the UV-to-near-IR wavelength regime. Our findings reinforce the results from Bell et al. (2012) who found no wavelength dependence for n across the rest-frame UV and optical wavelength regime for galaxies up to $z \sim 2.5$.

The absence of a striking wavelength dependence on the Sérsic index does not imply that light profiles do not systematically change with the wavelength. Galaxies have smaller-scale radii at longer wavelengths at both low and high redshift (Kelvin et al. 2012; van der Wel et al. 2014b). At low redshift we understand this to be due to gradients in attenuation (e.g., Popescu et al. 2000; Graham & Worley 2008) and stellar

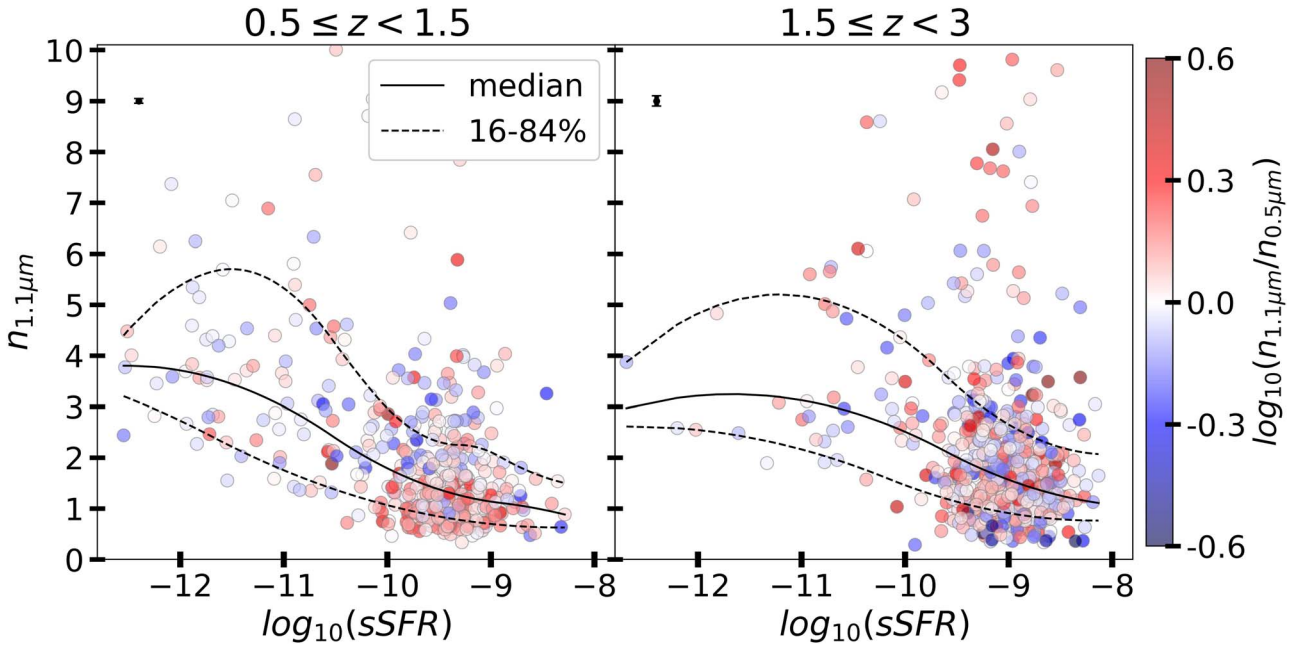

Figure 5. Sérsic index at 1.1 μm rest frame against the sSFR in two redshift bins, color coded with the ratio between the Sérsic indices at 1.1 μm and at 0.5 μm. The solid line shows the median for the whole sample in sSFR bins while the dashed lines show the 16–84th percentiles. In the upper left corner of each panel a black error bar shows the median uncertainty in $n_{1.1\mu m}$. Low-sSFR galaxies have systematically larger Sérsic indices in the rest-frame near-IR.

population properties (e.g., Sánchez-Blázquez et al. 2007; Zibetti et al. 2020). At large look-back time, thanks to JWST, such analysis is now becoming possible (Miller et al. 2022; Suess et al. 2022; Shen et al. 2023), and it is already clear that the stellar mass distribution is smoother (Wuyts et al. 2012) than the clumpier distribution seen in the UV and optical (e.g., Guo et al. 2015).

The key result presented here is that the radial profiles of star-forming and quiescent galaxies are different even in the rest-frame near-IR. If star formation and/or dust were responsible for the different structure seen at shorter wavelengths, then the Sérsic indices of star-forming and quiescent galaxies would become more similar at longer wavelengths. In fact, the reduced scatter in n of star-forming galaxies at longer wavelengths ($\lambda_{\rm rest} \approx 1.5\,\mu$m, see Figure 3) implies that the difference in structure is *more* pronounced in the rest-frame near-IR than the rest-frame UV/optical. The absence of such a trend implies, at first sight, that stellar mass profiles are similar to stellar light profiles, but as galaxy sizes decrease with the wavelength, and stellar half-mass radii are generally found to be smaller than half-light radii (e.g., Fang et al. 2013; Szomoru et al. 2013; Mosleh et al. 2017; Suess et al. 2017, 2019; Miller et al. 2023), the interpretation is not straightforward. Clearly, the outshining effect of young, bright, blue populations (Reddy et al. 2012; Wuyts et al. 2012; Lilly & Carollo 2016) plays a significant role. In particular, Fang et al. (2013) found that, for galaxies in the present-day Universe, the difference between half-mass and half-light radii is larger for star-forming galaxies than for quiescent galaxies and that stellar mass profiles in the range $3 < R < 10$ kpc are rather similar for quiescent and star-forming galaxies.

However, a high Sérsic index is driven by the combination of deviations from an exponential profile at both small radius, where Fang et al. (2013) indeed found a significant difference between the mass profiles of star-forming and quiescent galaxies, and large radius, which Fang et al. (2013) did not examine. In general, a decline in the galaxy size with the wavelength and a lack of such dependence for the Sérsic index are not necessarily in tension, and we conclude that there is a physical difference in the radial curvature of the stellar mass profiles when comparing star-forming and quiescent galaxies.

The strong correlation between the galaxy structure and star formation activity seen at high redshift (Franx et al. 2008; Wuyts et al. 2011; Bell et al. 2012; Barro et al. 2017; Whitaker et al. 2017) is now verified to be physical in nature and builds on well-documented correlations seen for present-day galaxies (e.g., Kauffmann et al. 2003; Brinchmann et al. 2004). A more in-depth discussion of the causal connection between structural evolution and star formation history/quenching (e.g., van der Wel et al. 2009; Bell et al. 2012; Fang et al. 2013; van Dokkum et al. 2015; Lilly & Carollo 2016; Tacchella et al. 2016; Barro et al. 2017; Bluck et al. 2020; Chen et al. 2020; Dimauro et al. 2022) is beyond the scope of this paper.

At $z \lesssim 1.5$, $M_* < 10^{10.3}\,M_\odot$ star-forming galaxies do show a *mild* increase in n with the wavelength, while this trend disappears at higher redshift. Because of the lack of a significant number of high-mass galaxies in the sample, we cannot argue the same for higher masses. However, the hint of a gradual trend of n with the redshift (Figure 6) at first sight echoes the usual line of thought that older bulges and a lack of attenuation in the center lead to an increased Sérsic index at longer wavelengths, but our measurements are not consistent with this picture. Instead, the trend is driven by galaxies with $M_* \lesssim 10^{10}\,M_\odot$, which display a slight *decrease* in n from high to low redshift in the rest-frame optical (mid row of Figure 6) while their rest-frame near-IR n shows a weaker and less significant evolution (top row of Figure 6). Similar trends were found at low redshift by Vulcani et al. (2014) and at $z \sim 2$–3 by Shibuya et al. (2015) comparing UV and optical wavelengths. We speculate that this is, at least partially, due to an increase in attenuation with cosmic time for galaxies in this mass range, associated with an increase in the gas-phase metallicity (e.g., Sanders et al. 2021).

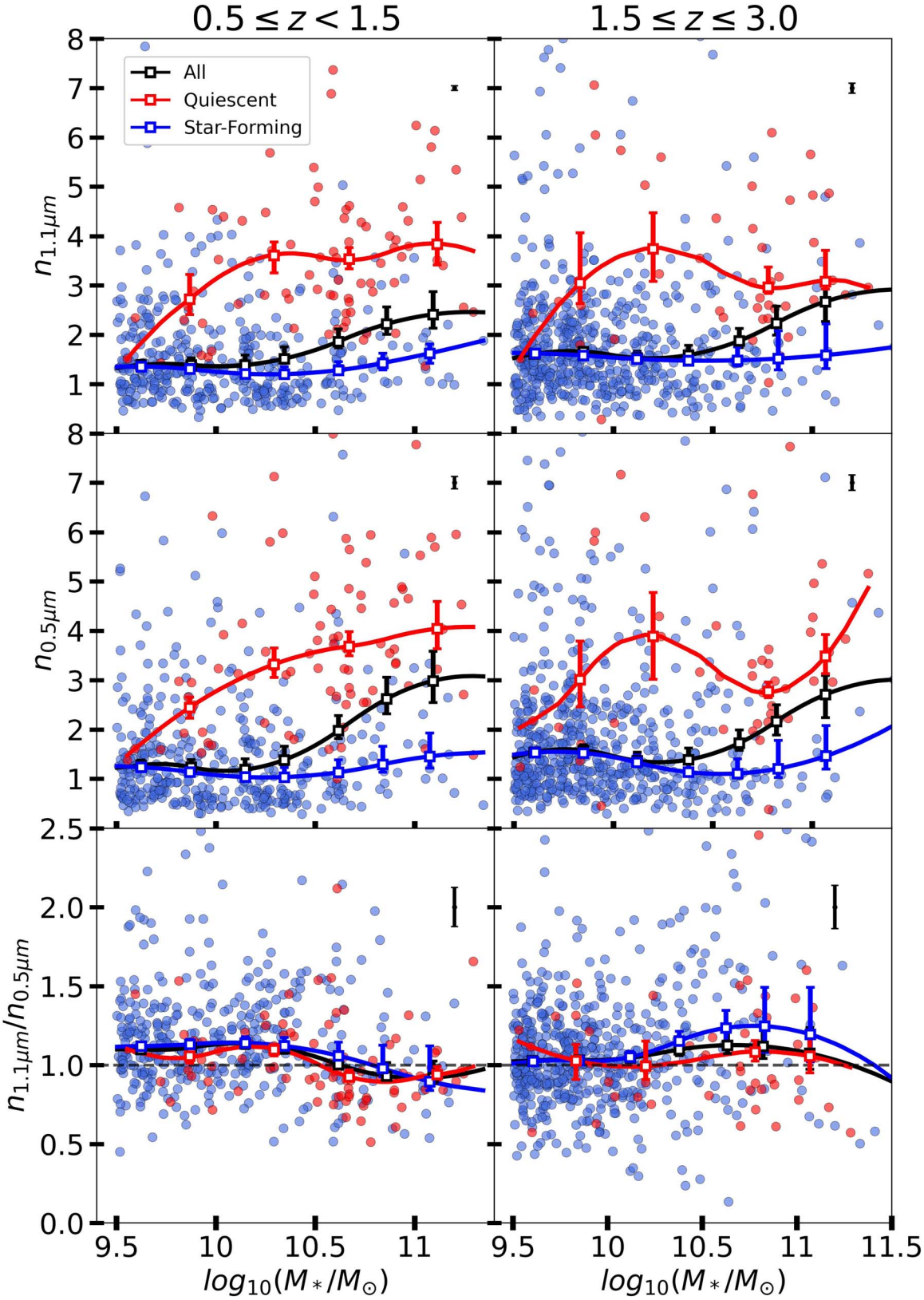

Figure 6. Sérsic indices at 1.1 μm (top row), 0.5 μm (mid row) and their ratio (bottom row) vs. the stellar mass, color coded as star-forming (blue) and quiescent (red). The left column shows galaxies at $0.5 \leqslant z < 1.5$; the right column shows galaxies at $1.5 \leqslant z \leqslant 3$. Blue and red lines show the medians for the star-forming and quiescent galaxies, respectively, while the black lines represent the full (combined) sample. Median lines are computed as described in Section 3.1 with a smoothing factor of 0.3 for the quiescent population and 1 for the star-forming and the whole sample. Error bars show the statistical uncertainty (84–16th percentiles $/\sqrt{N}$) in bins of width 0.5 dex for the quiescent population and 0.25 dex for the others. In the lower right corner of each panel a black error bar represents the median uncertainty for the whole sample. We see a clear dependence of n on the stellar mass, regardless of the wavelength and redshift, and no significant evidence for a mass- or redshift dependence for $n_{1.1\mu m}/n_{0.5\mu m}$.

5. Conclusions and Outlook

We present rest-frame optical and near-IR Sérsic index n measurements for a sample of 1067 galaxies at $0.5 < z < 3$ with stellar masses $M_* \geqslant 10^{9.5} M_\odot$ selected from recent JWST/NIRCam imaging that was collected as part of the CEERS program (Finkelstein et al. 2023). The wavelength dependence of n is weak (Figure 3). As a result, the near-IR light profiles of galaxies do not, on average, strongly differ from those in the optical (Figure 4). The large spread in n at any given wavelength is strongly correlated with the star formation activity (Figure 5), across the redshift and stellar mass. Indeed, after controlling for the star formation activity, star-forming galaxies show just a weak evolution in n with the redshift, as previously shown by Shibuya et al. (2015) in the rest-frame optical, and a mild dependence on the stellar mass. The remaining scatter is mostly driven by variations in the optical profile driven by dust absorption (Figure 4). Regardless of the wavelength, stellar mass, and redshift, we see that star-forming galaxies have $n \sim 1$–1.5, and quiescent galaxies have $n \sim 3.5$ (Figures 3 and 6).

The fact that the well-documented correlation between the galaxy structure and star formation activity (see Section 3.2) persists in the rest-frame near-IR implies a physical connection between the radial stellar mass distribution and growth through star formation. In other words, it is not a mere perception caused by young, bright, star-forming disks that fade after the cessation of star formation.

The lack of a strong wavelength dependence in the Sérsic index at all redshifts $z < 3$ also implies a plausible lack of such a dependence at even higher redshifts. As JWST/NIRCam explores the rest-frame optical up to $z \sim 10$ (Kartaltepe et al. 2023) and UV at $z > 10$, we can have some confidence that the observed radial light profiles inform us about the underlying stellar mass profiles even if M/L-gradient corrections are needed to reconstruct those.

Our conclusions hold for $0.1 < L/L_* < 1$ galaxies across the redshift range $0.5 < z < 3$ and the main weakness of the current study is the small number of high-mass star-forming galaxies (as discussed in Section 3.3), especially at high z. There are only 11(9) $M_* \geqslant 10^{11} M_\odot$ star-forming(quiescent) galaxies at $1.5 < z < 3$ investigated with JWST in our sample. For these galaxies the structure may be expected to vary the strongest with wavelength due to centrally concentrated, dust-obscured star formation activity. As larger areas are observed with the NIRCam by, for example, JADES (Williams et al. 2018), UNCOVER (Bezanson et al. 2022), and COSMOS-Web (Casey et al. 2023), this challenge will be addressed.

Acknowledgments

This project has received funding from the European Research Council (ERC) under the European Union's Horizon 2020 research and innovation program (grant agreement No. 683184). M.M. and M.B. acknowledge the financial support of the Flemish Fund for Scientific Research (FWO-Vlaanderen), research project G030319N.

Appendix
Sample Selection and Characteristics

Figure A1 shows the sample distribution and selection of galaxies used in this work. In the left panel we show the S/N in the HST/WFC3 filter F160W (empty circles) and JWST/NIRCam filter F150W (filled circles) as a function of the redshift. The dashed horizontal line shows the S/N = 50 limit suggested by van der Wel et al. (2012) to accurately measure Sérsic indices. The central panel of Figure A1 shows the mass distribution of our galaxies across the redshift. The right panel of the figure shows the sSFR against the redshift distribution of our galaxies. In the last two panels star-forming galaxies are color coded in blue while quiescent are red. The distinction between star-forming and quiescent is done as outlined in Section 3.1. We used circles for galaxies included in the sample and stars for galaxies that are rejected as outlined in Sections 2 and 2.2. Black squares represent galaxies that despite having an S/N < 50 in F150W are not removed from the sample.

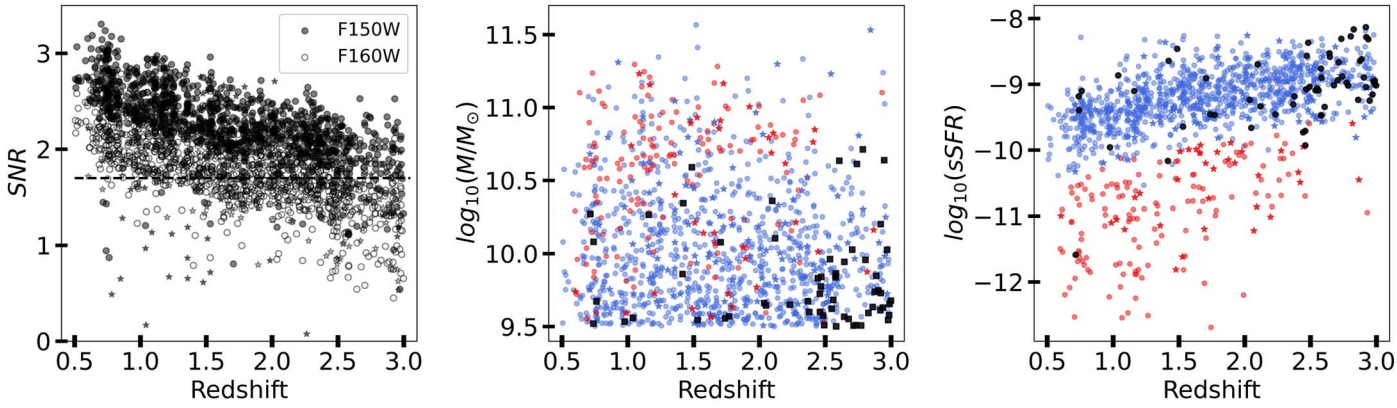

Figure A1. Left panel: S/N in the HST/ACS filter F160W (empty circles) and JWST/NIRCam F150W (filled circles) against redshift. The horizontal dashed black line shows the reference S/N = 50. Central panel: stellar mass against redshift. Right panel: sSFR against redshift. In the central and right panels red and blue colors are used to identify quiescent and star-forming galaxies. Circles define galaxies used in this work while stars show galaxies rejected according to Sections 2 and 2.2. Black squares are galaxies with S/N < 50 in F150W that are not rejected.

ORCID iDs

Marco Martorano https://orcid.org/0000-0003-2373-0404
Arjen van der Wel https://orcid.org/0000-0002-5027-0135
Eric F. Bell https://orcid.org/0000-0002-5564-9873
Marijn Franx https://orcid.org/0000-0002-8871-3026
Katherine E. Whitaker https://orcid.org/0000-0001-7160-3632
Angelos Nersesian https://orcid.org/0000-0001-6843-409X
Sedona H. Price https://orcid.org/0000-0002-0108-4176
Maarten Baes https://orcid.org/0000-0002-3930-2757
Katherine A. Suess https://orcid.org/0000-0002-1714-1905
Erica J. Nelson https://orcid.org/0000-0002-7524-374X
Tim B. Miller https://orcid.org/0000-0001-8367-6265
Rachel Bezanson https://orcid.org/0000-0001-5063-8254
Gabriel Brammer https://orcid.org/0000-0003-2680-005X

References

Baes, M., Nersesian, A., Casasola, V., et al. 2020, A&A, 641, A119
Barbary, K. 2016, JOSS, 1, 58
Barbary, K. 2018, SEP: Source Extraction and Photometry, Astrophysics Source Code Library, ascl:1811.004
Baringhaus, L., & Franz, C. 2004, J. Multivar. Anal., 88, 190
Barro, G., Faber, S. M., Koo, D. C., et al. 2017, ApJ, 840, 47
Bell, E. F., van der Wel, A., Papovich, C., et al. 2012, ApJ, 753, 167
Bertin, E., & Arnouts, S. 1996, A&AS, 117, 393
Bezanson, R., Labbe, I., Whitaker, K. E., et al. 2022, arXiv:2212.04026
Blanton, M. R., Hogg, D. W., Bahcall, N. A., et al. 2003, ApJ, 594, 186
Blanton, M. R., & Moustakas, J. 2009, ARA&A, 47, 159
Bluck, A. F. L., Maiolino, R., Sánchez, S. F., et al. 2020, MNRAS, 492, 96
Brammer, G. 2019, Grizli: Grism Redshift and Line Analysis Software, Astrophysics Source Code Library, ascl:1905.001
Brammer, G. B., Sánchez-Janssen, R., Labbé, I., et al. 2012, ApJL, 758, L17
Brinchmann, J., Charlot, S., White, S. D. M., et al. 2004, MNRAS, 351, 1151
Casey, C. M., Kartaltepe, J. S., Drakos, N. E., et al. 2023, ApJ, 954, 31
Chen, Z., Faber, S. M., Koo, D. C., et al. 2020, ApJ, 897, 102
Conselice, C. J. 2014, ARA&A, 52, 291
da Cunha, E., Charlot, S., & Elbaz, D. 2008, MNRAS, 388, 1595
Davis, M., Guhathakurta, P., Konidaris, N. P., et al. 2007, ApJL, 660, L1
de Jong, R. S. 1996a, A&A, 313, 45
de Jong, R. S. 1996b, A&A, 313, 377
Dimauro, P., Daddi, E., Shankar, F., et al. 2022, MNRAS, 513, 256
Driver, S. P., Norberg, P., Baldry, I. K., et al. 2009, A&G, 50, 5.12
Fang, J. J., Faber, S. M., Koo, D. C., & Dekel, A. 2013, ApJ, 776, 63
Finkelstein, S. L., Bagley, M. B., Ferguson, H. C., et al. 2023, ApJL, 946, L13
Finkelstein, S. L., Dickinson, M., Ferguson, H. C., et al. 2017, The Cosmic Evolution Early Release Science (CEERS) Survey, Cycle 0 Early Release Science JWST Proposal ID STScI, 1345
Franx, M., van Dokkum, P. G., Schreiber, N. M. F., et al. 2008, ApJ, 688, 770
Gillman, S., Gullberg, B., Brammer, G., et al. 2023, A&A, 676, A26
Graham, A. W., & Worley, C. C. 2008, MNRAS, 388, 1708
Grogin, N. A., Kocevski, D. D., Faber, S. M., et al. 2011, ApJS, 197, 35
Guo, Y., Ferguson, H. C., Bell, E. F., et al. 2015, ApJ, 800, 39
Häußler, B., Bamford, S. P., Vika, M., et al. 2013, MNRAS, 430, 330
Johnson, B., & Leja, J. 2017, Bd-J/Prospector: Initial Release, v0.1, Zenodo, doi:10.5281/zenodo.1116491
Johnson, B. D., Leja, J., Conroy, C., & Speagle, J. S. 2021, ApJS, 254, 22
Kartaltepe, J. S., Rose, C., Vanderhoof, B. N., et al. 2023, ApJL, 946, L15
Kauffmann, G., Heckman, T. M., White, S. D. M., et al. 2003, MNRAS, 341, 33
Kelvin, L. S., Driver, S. P., Robotham, A. S. G., et al. 2012, MNRAS, 421, 1007
Kennedy, R., Bamford, S. P., Baldry, I., et al. 2015, MNRAS, 454, 806
Koekemoer, A. M., Faber, S. M., Ferguson, H. C., et al. 2011, ApJS, 197, 36
Lang, P., Wuyts, S., Somerville, R. S., et al. 2014, ApJ, 788, 11
Lawrence, A., Warren, S. J., Almaini, O., et al. 2007, MNRAS, 379, 1599
Lawrence, A., Warren, S. J., Almaini, O., et al. 2012, VizieR On-line Data Catalog: II/314, yCat, 2314, 0
Leja, J., Speagle, J. S., Johnson, B. D., et al. 2020, ApJ, 893, 111
Leja, J., Speagle, J. S., Ting, Y.-S., et al. 2022, ApJ, 936, 165
Lilly, S. J., & Carollo, C. M. 2016, ApJ, 833, 1
Miller, T. B., van Dokkum, P., & Mowla, L. 2023, ApJ, 945, 155
Miller, T. B., Whitaker, K. E., Nelson, E. J., et al. 2022, ApJL, 941, L37
Mosleh, M., Tacchella, S., Renzini, A., et al. 2017, ApJ, 837, 2
Naidu, R. P., Oesch, P. A., van Dokkum, P., et al. 2022, ApJL, 940, L14
Nardiello, D., Bedin, L. R., Burgasser, A., et al. 2022, MNRAS, 517, 484
Nedkova, K. V., Häußler, B., Marchesini, D., et al. 2021, MNRAS, 506, 928
Nelson, E. J., van Dokkum, P. G., Momcheva, I. G., et al. 2016, ApJL, 817, L9
Nersesian, A., Zibetti, S., D'Eugenio, F., & Baes, M. 2023, A&A, 673, A63
Ng, P., & Maechler, M. 2007, Stat. Model., 7, 315
Ng, P., & Maechler, M. 2022, COBS—Constrained B-splines (Sparse Matrix based), https://CRAN.R-project.org/package=cobs
Papovich, C., Labbé, I., Quadri, R., et al. 2015, ApJ, 803, 26
Pastrav, B. A., Popescu, C. C., Tuffs, R. J., & Sansom, A. E. 2013, A&A, 553, A80
Peng, C. Y., Ho, L. C., Impey, C. D., & Rix, H.-W. 2002, AJ, 124, 266
Peng, Y.-j., Lilly, S. J., Kovač, K., et al. 2010, ApJ, 721, 193
Popescu, C. C., Misiriotis, A., Kylafis, N. D., Tuffs, R. J., & Fischera, J. 2000, A&A, 362, 138
Reddy, N. A., Pettini, M., Steidel, C. C., et al. 2012, ApJ, 754, 25
Rieke, M. J., Kelly, D., & Horner, S. 2005, Proc. SPIE, 5904, 1
Sánchez-Blázquez, P., Forbes, D. A., Strader, J., Brodie, J., & Proctor, R. 2007, MNRAS, 377, 759
Sanders, R. L., Shapley, A. E., Jones, T., et al. 2021, ApJ, 914, 19
Shen, L., Papovich, C., Yang, G., et al. 2023, ApJ, 950, 7
Shibuya, T., Ouchi, M., & Harikane, Y. 2015, ApJS, 219, 15
Skelton, R. E., Whitaker, K. E., Momcheva, I. G., et al. 2014, ApJS, 214, 24
Suess, K. A., Bezanson, R., Nelson, E. J., et al. 2022, ApJL, 937, L33
Suess, K. A., Bezanson, R., Spilker, J. S., et al. 2017, ApJL, 846, L14
Suess, K. A., Kriek, M., Price, S. H., & Barro, G. 2019, ApJL, 885, L22
Szomoru, D., Franx, M., van Dokkum, P. G., et al. 2013, ApJ, 763, 73
Tacchella, S., Conroy, C., Faber, S. M., et al. 2022, ApJ, 926, 134
Tacchella, S., Dekel, A., Carollo, C. M., et al. 2016, MNRAS, 458, 242
Tal, T., Dekel, A., Oesch, P., et al. 2014, ApJ, 789, 164
van der Wel, A., Bell, E. F., Häussler, B., et al. 2012, ApJS, 203, 24
van der Wel, A., Bell, E. F., van den Bosch, F. C., Gallazzi, A., & Rix, H.-W. 2009, ApJ, 698, 1232
van der Wel, A., Chang, Y.-Y., Bell, E. F., et al. 2014a, ApJL, 792, L6
van der Wel, A., Franx, M., van Dokkum, P. G., et al. 2014b, ApJ, 788, 28
van Dokkum, P. G., Nelson, E. J., Franx, M., et al. 2015, ApJ, 813, 23
Vika, M., Bamford, S. P., Häußler, B., et al. 2013, MNRAS, 435, 623
Vulcani, B., Bundy, K., Lackner, C., et al. 2014, ApJ, 797, 62
Weaver, J. R., Cutler, S. E., Pan, R., et al. 2023, arXiv:2301.02671
Whitaker, K. E., Bezanson, R., van Dokkum, P. G., et al. 2017, ApJ, 838, 19
Whitaker, K. E., Franx, M., Leja, J., et al. 2014, ApJ, 795, 104
Whitney, A., Ferreira, L., Conselice, C. J., & Duncan, K. 2021, ApJ, 919, 139
Williams, C. C., Curtis-Lake, E., Hainline, K. N., et al. 2018, ApJS, 236, 33
Wuyts, S., Förster Schreiber, N. M., Genzel, R., et al. 2012, ApJ, 753, 114
Wuyts, S., Förster Schreiber, N. M., van der Wel, A., et al. 2011, ApJ, 742, 96
Yao, Y., Song, J., Kong, X., et al. 2023, ApJ, 954, 113
Zhuang, M.-Y., & Shen, Y. 2023, arXiv:2304.13776
Zibetti, S., Gallazzi, A. R., Hirschmann, M., et al. 2020, MNRAS, 491, 3562